Practical Application of Two-Turning-Point Theory to Mountain-Wave Transmission through a Wind Jet

DAVE BROUTMAN

Computational Physics, Inc., Springfield, Virginia

STEPHEN D. ECKERMANN

Space Science Division, Naval Research Laboratory, Washington, D.C.

JAMES W. ROTTMAN

Naval Hydrodynamics Division, Science Applications International Corporation, San Diego, California

ABSTRACT

A Fourier method is used to model mountain waves that have nearby turning points in a wind jet. In Fourier space, the propagation equations are solved by ray theory. To correct for the ray singularity at a turning point without time-consuming special-function evaluations, the ray solution is linearly interpolated across the breakdown region. The Fourier solutions for the spatial wavefield are compared with mesoscale model simulations in two cases: two-dimensional flow over idealized topography with uniform stratification and a sech-squared wind profile and three-dimensional flow over the island of Jan Mayen with stratification and wind profiles taken from radiosonde measurements. The latter case reveals the partial transmission of trapped mountain waves into the stratosphere.

1. Introduction

Mountain waves propagate to great heights in the atmosphere (see the review by Fritts and Alexander 2003), at times reaching the mesosphere and lower thermosphere (Bacmeister 1993; Eckermann et al. 2007). The propagation can be interrupted by wind jets, which produce evanescent layers that partially reflect and partially transmit the waves (e.g., Nault and Sutherland 2008, hereafter NaSu). Above the wind jet, the partially transmitted waves can continue to grow with height in response to the decreasing air density and can make an important contribution to the wavefield at higher altitudes (see the numerical simulations in Eckermann et al. 2006, hereafter EB06).

Here we use a Fourier method to model mountain waves in the presence of a wind jet. In Fourier space the theory is one-dimensional, and the solution can be computed efficiently by ray theory, although ray theory breaks down near turning points. For a single isolated turning point, the solution is efficiently calculated with an Airy function, but in the cases we consider here there are as many as four nearby turning points in the wind jet. The solution for just two nearby turning points involves Weber (or parabolic cylinder) functions and is very slow computationally.

We aim for computation times of minutes for the entire Fourier spectrum, as has been achieved (without the treatment of nearby turning points) in previous applications of Fourier methods to mountain waves (Broutman et al. 2003; EB06). Efficiency is important because in realistic three-dimensional cases there can be many thousands of Fourier components with nearby turning points in the wind jet.

We find that an efficient but approximate solution in the region of nearby turning points is obtained by linearly interpolating the ray solution across the turning-point region. No special functions are evaluated, but it is necessary to have a reliable estimate for where ray

Corresponding author address: Stephen Eckermann, Space Science Division, Naval Research Laboratory, Code 7646, Washington, DC 20375.
E-mail: stephen.eckermann@nrl.navy.mil

				Form Approved
Report Documentation Page				*OMB No. 0704-0188*

Public reporting burden for the collection of information is estimated to average 1 hour per response, including the time for reviewing instructions, searching existing data sources, gathering and maintaining the data needed, and completing and reviewing the collection of information. Send comments regarding this burden estimate or any other aspect of this collection of information, including suggestions for reducing this burden, to Washington Headquarters Services, Directorate for Information Operations and Reports, 1215 Jefferson Davis Highway, Suite 1204, Arlington VA 22202-4302. Respondents should be aware that notwithstanding any other provision of law, no person shall be subject to a penalty for failing to comply with a collection of information if it does not display a currently valid OMB control number.

1. REPORT DATE **18 JUL 2008**	2. REPORT TYPE	3. DATES COVERED **00-00-2008 to 00-00-2008**

4. TITLE AND SUBTITLE **Practical Application of Two-Turning-Point Theory to Mountain-Wave Transmission through a Wind Jet**	5a. CONTRACT NUMBER
	5b. GRANT NUMBER
	5c. PROGRAM ELEMENT NUMBER
6. AUTHOR(S)	5d. PROJECT NUMBER
	5e. TASK NUMBER
	5f. WORK UNIT NUMBER
7. PERFORMING ORGANIZATION NAME(S) AND ADDRESS(ES) **Naval Research Laboratory,Space Science Division,Washington,DC,20375**	8. PERFORMING ORGANIZATION REPORT NUMBER
9. SPONSORING/MONITORING AGENCY NAME(S) AND ADDRESS(ES)	10. SPONSOR/MONITOR'S ACRONYM(S)
	11. SPONSOR/MONITOR'S REPORT NUMBER(S)

12. DISTRIBUTION/AVAILABILITY STATEMENT
Approved for public release; distribution unlimited

13. SUPPLEMENTARY NOTES

14. ABSTRACT

A Fourier method is used to model mountain waves that have nearby turning points in a wind jet. In Fourier space, the propagation equations are solved by ray theory. To correct for the ray singularity at a turning point without time-consuming special-function evaluations, the ray solution is linearly interpolated across the breakdown region. The Fourier solutions for the spatial wavefield are compared with mesoscale model simulations in two cases: two-dimensional flow over idealized topography with uniform stratification and a sech-squared wind profile and three-dimensional flow over the island of Jan Mayen with stratification and wind profiles taken from radiosonde measurements. The latter case reveals the partial transmission of trapped mountain waves into the stratosphere.

15. SUBJECT TERMS

16. SECURITY CLASSIFICATION OF:			17. LIMITATION OF ABSTRACT	18. NUMBER OF PAGES	19a. NAME OF RESPONSIBLE PERSON
a. REPORT **unclassified**	b. ABSTRACT **unclassified**	c. THIS PAGE **unclassified**	**Same as Report (SAR)**	**14**	

theory breaks down near the turning points. This indicates where to start and stop the interpolation. The criterion is discussed in section 3d.

We first test the interpolated ray solution for selected Fourier components using a sech-squared mean wind profile and constant stratification. We consider cases in which the curvature of the wind profile is ignored and included in the theory. When ignored, the maximum number of turning points per Fourier component is two. When included, the maximum number is four. We do not have a four-turning-point theory, so we attempt, with some success, to model four turning points with the two-turning-point theory.

We then calculate spatial solutions for the mountain waves by a Fourier superposition of the ray solutions. We start with two-dimensional mountain waves generated by idealized topography, a sech-squared wind profile, and uniform stratification. We then consider three-dimensional mountain waves generated by the island of Jan Mayen, with stratification and wind profiles taken from radiosonde measurements over the island.

The Jan Mayen case has been examined by EB06. Their Fourier solution did not include the treatment of nearby turning points and did not accurately reproduce the results of a mesoscale model simulation at heights above the wind jet, centered near 10-km altitude. From estimates of the integral given here by Q in (7), these authors suggested that there would be significant wave transmission through the jet region. We repeat their Fourier calculation, but we include the treatment of nearby turning points. We find an improved comparison between the solutions of the Fourier method and the mesoscale model.

In quantum mechanics, the evanescent region between turning points is called a potential barrier, and wave transmission through a potential barrier is called tunneling. Our four-turning-point case is an example of a double potential barrier. Analogies to quantum mechanical tunneling for gravity waves are discussed in Sutherland and Yewchuk (2004) and Brown and Sutherland (2007). These authors derive analytic wave solutions using piecewise constant profiles for the background stratification and shear. Further work on gravity wave tunneling by Nault and Sutherland (2007) and NaSu is based on the numerical integration of an equation similar to (1) below and will be discussed in the concluding section of our paper.

We formulate the problem in section 2, derive two-turning-point solutions in section 3, consider the effects of wind curvature in section 4, and introduce other effects needed for mountain-wave simulations in section 5. An idealized case with a sech-squared wind profile is given in section 6. A realistic case for Jan Mayen is given in section 7, followed by a discussion in section 8.

2. Formulation

We consider stationary mountain waves propagating in a background that depends on height z. The mean buoyancy frequency is $N(z)$. The mean wind has components $U(z)$, $V(z)$ in the horizontal directions x, y, respectively. Initially, the Boussinesq approximation is made. In section 5c we add the usual anelastic density scaling for the wave amplitudes.

The mountain waves have horizontal wavenumber components k, l in x, y respectively, and intrinsic frequency $\hat{\omega} = -kU - lV$. The vertical velocity for a particular Fourier component, $\tilde{w}(k, l, z)$, satisfies

$$\tilde{w}_{zz} + m^2(z)\tilde{w} = 0, \qquad (1)$$

where (see Teixeira et al. 2004)

$$m^2 = k_h^2(N^2/\hat{\omega}^2 - 1) + \alpha(kU_{zz} + lV_{zz})/\hat{\omega} \qquad (2)$$

and $k_h = (k^2 + l^2)^{1/2}$. In the anelastic approximation, a term $-1/4H_d^2$ is added to the right-hand side of (2), where H_d is the density scale height (e.g., NaSu). We ignore this term, which is small for the horizontal wavelengths of importance here (10–50 km).

The value of α in (2) will be set to unity or zero, respectively, to include or omit wind curvature terms. When $\alpha = 0$, (2) is the dispersion relation for internal gravity waves and m is the vertical wavenumber. It can be shown that the vertical group velocity is positive when m and $\hat{\omega}$ have the opposite sign, and thus when m and $kU + lV$ have the same sign. Our notation is that m is positive (negative) for upgoing (downgoing) wave groups. This is opposite to the sign notation often used for gravity waves, but we have chosen it to simplify the application of two-turning-point theories. These were developed in other contexts and are typically formulated so that the wavenumber is positive for waves that are incident upon and transmitted through the turning-point region.

The topography has elevation $h(x, y)$. The linearized lower boundary condition for mountain waves is [cf. Eq. (5.2.4) in Baines 1995]

$$\tilde{w} = -i\hat{\omega}\tilde{h}, \qquad (3)$$

evaluated at $z = 0$, where $\tilde{h}(k, l)$ is the Fourier transform of $h(x, y)$.

An inverse Fourier transform of $\tilde{w}(k, l, z)$ gives the spatial solution:

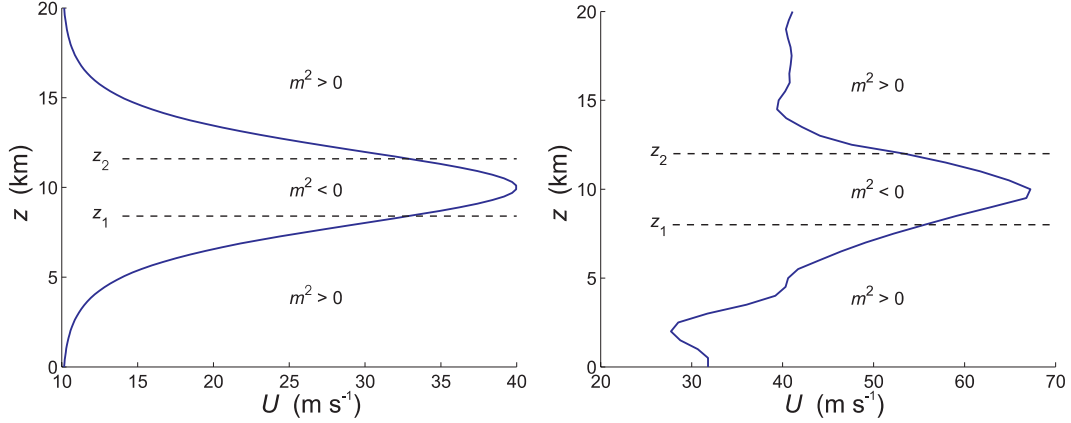$$w(x, y, z) = \int\limits_{-\infty}^{\infty}\int \tilde{w}(k, l, z)e^{\iota(kx+ly)}dk\,dl. \qquad (4)$$

FIG. 1. Wind profiles used in the present paper: (left) the sech-squared profile in (26); (right) the westerly component of the wind obtained from radiosonde measurements and used (along with a weaker north–south component) in EB06. Turning points for a particular Fourier component are indicated at heights z_1 and z_2. They separate propagating regions ($m^2 > 0$) from evanescent regions ($m^2 < 0$).

3. Two-turning-point theory

We first consider the solution for Fourier components with two turning points. Figure 1 illustrates the problem for the two wind profiles used in this study: a sech-squared profile and the wind profile measured above Jan Mayen. The turning point heights z_1 and z_2, with $z_1 < z_2$, are functions of k, l as well as of U, V, and N.

We examine three solutions to (1): the ray solution, a uniformly valid solution, and a solution by numerical integration.

a. The ray solution

The ray solution for (1) is derived by assuming that the vertical wavenumber m is a slowly varying function of height. The derivation also yields a solution in evanescent regions, where m is imaginary, but it diverges at turning points, where $m = 0$. We will refer to this as the ray solution even though it includes regions of evanescence. We might have called it a phase integral solution (as in Fröman and Fröman 2002 and Heading 1962), but this term is less familiar and does not reflect our use of ray theory to incorporate wave transience (see section 5). The term "WKBJ solution" is sometimes used, but this is often meant to imply that the ray solution has been matched to a special-function solution near the turning point. We have not done the matching but will instead compute a uniformly valid expression from the ray solution (see section 3b).

The ray solution used here is derived in Fröman and Fröman (1965, 1970). We define the phase integrals

$$q_1(z) = \int_{z_1}^{z} m\,dz, \tag{5}$$

$$q_2(z) = \int_{z_2}^{z} m\,dz, \quad \text{and} \tag{6}$$

$$Q = \int_{z_1}^{z_2} |m|\,dz. \tag{7}$$

Note that below the lower turning point, $z < z_1$, we have from (5) negative q_1 but positive dq_1/dz. Thus, in the following ray solutions we associate $\pm q_1$ with, respectively, upgoing and downgoing wave groups below the lower turning point.

The ray solutions are

$$\tilde{w}_t = Cm^{-1/2}e^{i(q_2+\pi/4)}, \tag{8}$$

$$\tilde{w}_r = C|m|^{-1/2}e^{Q}e^{-i(q_1+\pi/4)}, \quad \text{and} \tag{9}$$

$$\tilde{w}_i = Cm^{-1/2}(e^{2Q}+1)^{1/2}e^{i(q_1+\pi/4+2\sigma)}, \tag{10}$$

where C is a constant determined by a boundary condition. The subscripts t, r, and i refer, respectively, to the transmitted wave ($z > z_2$) and the reflected and incident waves ($z < z_1$). The phase shift 2σ can be ignored except when the two turning points are close to each other. It is at most about 10°, as noted in Berry and Mount (1972). An expression for σ is given by Fröman and Dammert [1970, Eq. (57)]:

$$\sigma = 0.5[Q^* \log Q^* - Q^* + \arg \Gamma(0.5 - iQ^*)], \tag{11}$$

where $Q^* = Q/\pi$ and Γ is the gamma function.

Thus,

$$\tilde{w}(z) = \tilde{w}_i + \tilde{w}_r \quad \text{for} \quad z < z_1, \quad \text{and} \tag{12}$$

$$\tilde{w}(z) = \tilde{w}_t \quad \text{for} \qquad z > z_2. \qquad (13)$$

The upper boundary condition is a radiation condition, satisfied by the form chosen for $\tilde{w}_t$, which represents an outgoing wave.

Note that the ray solution for the transmitted wave can be derived without matching the ray solution to a special-function solution valid in the turning-point region. The relation between the ray solution above the turning-point region ($z > z_2$) and the ray solution below the turning-point region ($z < z_1$) can instead be found by following the ray solution through the complex z plane on a path that avoids the turning points. This use of the complex plane was suggested soon after the original WKB papers were published in the 1920s. For more history and explanation, see Fröman and Fröman (2002) and Heading (1962).

Between the two turning points, where m is imaginary, we use the evanescent WKB solution [see Fröman and Fröman 1965, Eq. (9.20b)]:

$$\tilde{w}(z) = C|m|^{-1/2} e^{-|q_2|} \quad \text{for} \quad z_1 < z < z_2. \qquad (14)$$

This single-exponential form is only valid in the limit of well-separated turning points and represents the lowest-order WKB solution. Like the ray solutions in (8)–(10), solution (14) diverges at each turning point and is inaccurate at distances close to each turning point.

b. The uniformly valid solution

A uniformly valid solution can be derived that approximates the ray solution far from the turning points and is also accurate near the turning points. For a single turning point, the uniform solution involves the Airy function (e.g., Berry and Mount 1972). For two turning points, the uniform solution involves the parabolic cylinder function (Berry and Mount 1972; Razavy 2003), which is a solution to the parabolic cylinder equation (Abramowitz and Stegun 1964, hereafter AS64, section 19.16)

$$W_{z'z'} + (z'^2/4 - a)W = 0. \qquad (15)$$

Here, z' is a nondimensional height coordinate, and the two turning points are located at $z' = \pm 2a^{1/2}$. Equation (15) has a coefficient that is symmetric and parabolic in z', the simplest form of our original Eq. (1) with a smooth coefficient and two turning points. Although parabolic, the solutions to (15) can be scaled to approximate the solution for more general two-turning-point coefficients that are not parabolic, except in the close vicinity of the turning points.

Two independent solutions of (15) are given by AS64 as $E(a, z')$ and its complex conjugate $E^*(a, z')$. Only $E(a, z')$ satisfies the radiation condition at $z' \gg a$. In this limit, we have [from AS64, Eq. (19.21.1)]

$$E(a, z') \sim (2/z')^{1/2} e^{i(z'^2/4 - a\log z' + \phi_2/2 + \pi/4)}, \qquad (16)$$

where $\phi_2 = \arg \Gamma(1/2 + ia)$. The derivative with respect to z' of the imaginary part of the exponent in (16) gives a wavenumber $m \sim z'/2 - a/z'$. Thus, $m > 0$ for $z' \gg a$, and E represents an upward-propagating wave group above the second turning point.

For negative z', we evaluate E from AS64's Eq. (19.18.3):

$$iE(a, -z') = -(1 + e^{2\pi a})^{1/2} E^*(a, z') + e^{\pi a} E(a, z'). \quad (17)$$

This expression is for $z' > 0$, so E on the left-hand side above has a negative second argument. For (15), the integral in (7) is $Q = \pi a$. Comparing the exponential terms in (17) to the Q terms in the ray solutions (9)–(10), we identify the first term in (17) as the incident wave and the second term as the reflected wave.

The idea of the uniform solution (e.g., Berry and Mount 1972) is to adjust the size and shape of $E(a, z')$ so that it approximates the solution of a more general two-turning-point equation. This adjustment involves only quantities that are used in the ray solution (Berry 1969), such as the phase integral $\int m \, dz$ that appears in (8)–(10).

To simplify the expressions below, we define

$$\zeta = z'/2^{1/2} \quad \text{and} \quad b = (2a)^{1/2}. \qquad (18)$$

This transforms the parabolic cylinder Eq. (15) to

$$W_{\zeta\zeta} + (\zeta^2 - b^2)W = 0, \qquad (19)$$

which Kravtsov and Orlov (1999) call Weber's equation. The turning points are at $\zeta = \pm b$.

The uniform solution for (1) has the form (Kravtsov and Orlov 1999)

$$\tilde{w}(z) = DA(z)E[b, \zeta(z)], \qquad (20)$$

where D is a constant used to satisfy the lower boundary condition, and

$$A(z) = [(\zeta^2(z) - b^2)/m^2(z)]^{1/4}, \qquad (21)$$

$$b = 2Q/\pi. \qquad (22)$$

The mapping $\zeta(z)$ is defined by the following integrals. [Note that this is the mapping $\zeta(z)$, where z is our height coordinate, not $\zeta(z')$ of (18), where z' is the coordinate in the parabolic cylinder Eq. (15).] For $z < z_1$,

$$\int_{\zeta}^{-b} (\zeta^2 - b^2)^{1/2} d\zeta = \int_{z}^{z_1} m\, dz. \qquad (23)$$

For $z_1 < z < z_2$,

$$\int_{-b}^{\zeta} (b^2 - \zeta^2)^{1/2} d\zeta = \int_{z_1}^{z} |m|\, dz. \qquad (24)$$

For $z > z_2$,

$$\int_{b}^{\zeta} (\zeta^2 - b^2)^{1/2} d\zeta = \int_{z_2}^{z} m\, dz. \qquad (25)$$

The turning points $z = z_1$ and $z = z_2$ are mapped to $\zeta = -b$ and $\zeta = b$, respectively. The integrals on the left-hand side of the above three equations can be evaluated analytically, but the integrals on the right-hand side generally need numerical solution. Also, the explicit relation for $\zeta(z)$ needs to be determined iteratively.

c. Solutions for a sech-squared wind profile

We consider the wind profile shown in the left panel of Fig. 1:

$$U = U_0 + U_1 \operatorname{sech}^2[(z - z_m)^2 / L^2], \qquad (26)$$

with $U_0 = 10 \text{ m s}^{-1}$, $U_1 = 30 \text{ m s}^{-1}$, $z_m = 10$ km, and $L = 3$ km. The other background profiles are $V = 0$ and $N = 0.015 \text{ s}^{-1}$.

For now, we ignore the wind curvature terms, setting $\alpha = 0$ in (1). There are then at most two turning points, symmetrically located below and above $z = z_m$.

All numerical results in the present paper were produced with Matlab version 7.4. The phase integrals in the ray solution, (5)–(7), and the integrals in the uniform solution, (23)–(25), were approximated by the trapezoidal rule. The iterative solution to (23)–(25) was obtained using Matlab's root-finding routine fzero. The parabolic cylinder function in (20) was evaluated using Matlab's generalized hypergeometric function routine. The numerical solution to (1) was obtained with Matlab's ordinary differential equation solver ode23, with default error tolerances of 10^{-3} for the relative error and 10^{-6} for the absolute error.

Figure 2 shows the ray and uniform solutions of (1), along with a solution by numerical integration (see below). The left and right panels are for a horizontal wavelength of 16.3 and 14 km, respectively. The solutions were computed at 100 evenly spaced heights from 0 to 20 km. The ray solution diverges at both turning points, whose heights are denoted in the figure by horizontal dotted lines. The computed values are finite because the discrete grid points miss the turning points slightly.

The numerical solution to (1) was calculated with an initial condition given by the transmitted ray solution (8) at $z = 20$ km. This was then integrated downward to $z = 0$. The numerical solution separates slightly from the uniform solution as the integration proceeds downward through the evanescent region between the turning points, although the agreement is still quite good below the wind jet. We repeated the numerical integration with much smaller error tolerances, but the result was the same. The small discrepancy between the numerical and ray solutions may thus be due to errors in the ray approximation. Higher-order corrections to the ray solution can be computed by the method of Fröman and Fröman (2002) but were not attempted here.

In our calculations, the ray solution was by far the fastest to compute. The numerical solution took over 10 times longer, and the uniform solution took over 100 times longer (about a couple of seconds on a 1-GHz processor). Most of the computation time for the uniform solution was spent evaluating the parabolic cylinder function E in (20), although the iterative solution for the mappings (23)–(25) by itself took 10 times longer than the ray calculation. We experimented somewhat with parameter settings in the Matlab routines, and the above comments refer to our best times. There may be much faster algorithms for evaluating the parabolic cylinder function.

In the Jan Mayen example reported below, we need to compute two-turning-point solutions for thousands of horizontal wavenumbers. To do this with reasonable speed, we use the ray method and introduce a simple modification to correct its breakdown near the turning points, as we now discuss.

d. The interpolated ray solution

We first identify the region of ray-theory breakdown using the following quantity, which measures the slow variation of the vertical wavenumber m:

$$\epsilon = \frac{1}{|m|^2} \left| \frac{3}{4} \left(\frac{1}{m} \frac{dm}{dz} \right)^2 - \frac{1}{2m} \frac{d^2m}{dz^2} \right| \qquad (27)$$

$$= \frac{1}{16m^6} \left| 5 \left(\frac{dm^2}{dz} \right)^2 - 4m^2 \frac{d^2 m^2}{dz^2} \right|. \qquad (28)$$

Ray methods are asymptotically valid; that is, their accuracy improves as $\epsilon \to 0$. At a turning point, ϵ diverges because neighboring rays with slightly different values
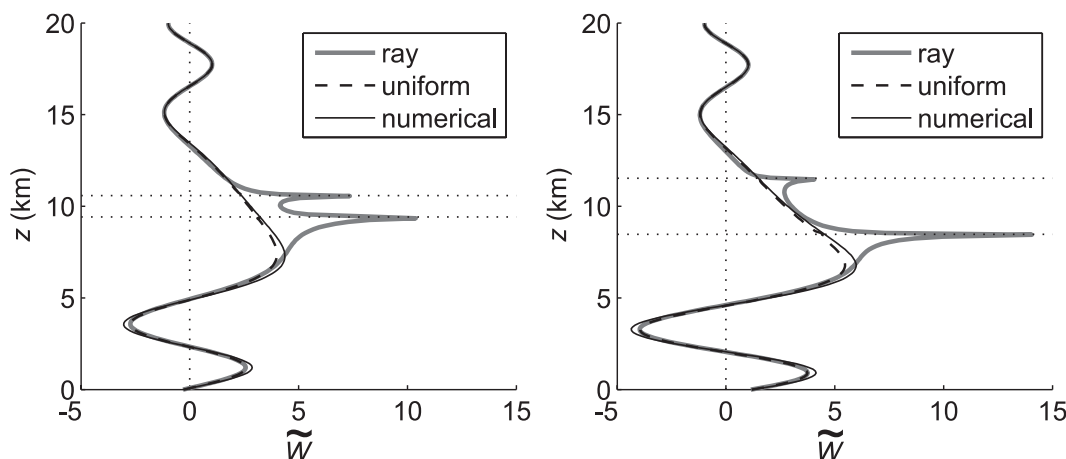
FIG. 2. Solutions for $\tilde{w}$ for the sech-squared wind profile (26) for (left) horizontal wavelength 16.3 km, $z_1 = 9.4$ km, and $z_2 = 10.6$ km and (right) horizontal wavelength 14 km, $z_1 = 8.2$ km, and $z_2 = 11.8$ km. Horizontal dotted lines indicate the turning-point heights z_1, z_2. The solutions are normalized so that $\tilde{w} = -1$ at $z = 20$ km, and the real part of $\tilde{w}$ is plotted. Note that these are Boussinesq solutions. Anelastic scalings are added in section 5c.

of m cross each other. This results in the divergence of the derivatives in the above expressions.

The above expressions are taken from Fröman and Fröman [1965, Eq. (3.5)]. The first form, (27), is also given by Einaudi and Hines (1970). The second form, (28), is in terms of m^2, which is real for all real z.

We consider ray theory to be sufficiently accurate wherever $\epsilon < 1$, and we leave the ray solution as it is at those heights. At heights where $\epsilon > 1$, we replace the ray solution with linear interpolated values across those heights. Let $z = r$ and $z = s$ be heights on either side of a region where $\epsilon > 1$. Our modification to the ray solution is then given by the linear interpolation

$$\tilde{w}(r < z < s) \rightarrow \tilde{w}(r) + (z - r)\frac{\tilde{w}(s) - \tilde{w}(r)}{s - r}. \qquad (29)$$

We show examples of the interpolated ray solution (indicated by thick dashed lines) in Fig. 3. The two upper panels are the same cases as the respective panels of Fig. 2. We approximated ϵ using centered differences for the derivatives of m^2 in (28).

The lower left panel of Fig. 3 shows the least accurate result we found using the interpolated ray method for the present wind profile, ignoring wind curvature. Here ϵ reaches a local minimum of about 0.8 near the middle of the wind jet at $z = 10$ km (bottom right panel). We experimented with other values of ϵ for determining ray theory validity, but the value of unity usually led to the best approximation. A possible improvement to our procedure might be to interpolate across the entire evanescent region when the turning points are sufficiently close.

4. Wind curvature

Next we include the previously omitted wind curvature terms by setting $\alpha = 1$ in (2). The difficulty is that some Fourier components now have four nearby turning points in the wind jet. We do not know the relevant special functions for four nearby turning points, but their computation is likely to be too time-consuming anyway for our purposes.

So instead we model four turning points using the interpolated ray solution for two turning points. Three examples, each with a different horizontal wavelength λ, are shown in Fig. 4. The left panels show $\tilde{w}$, and the right panels show the corresponding m^2 profile. For comparison, m^2 is also plotted without wind curvature terms. With wind curvature, the m^2 curve has two minima and more closely straddles the $m^2 = 0$ axis in the region of the turning points.

The initial condition for these calculations is an upgoing plane wave of unit amplitude at $z = 20$ km. In the upper two rows of Fig. 4, the numerical solution and the interpolated ray solution agree closely.

The agreement is not always so good. This is illustrated in the bottom row of Fig. 4, where the interpolated ray solution below the wind jet has an amplitude that is about half that of the numerical solution, although the phases agree well. There are only two turning points in this case, with m^2 not quite crossing over to positive values near $z = 10$ km. The reason that the two-turning-point theory is not accurate for this two-turning-point case is that it assumes a locally quadratic shape for m^2 near the turning points rather than the quartic shape realized here. On the other hand, we should not have expected the two-turning-point theory
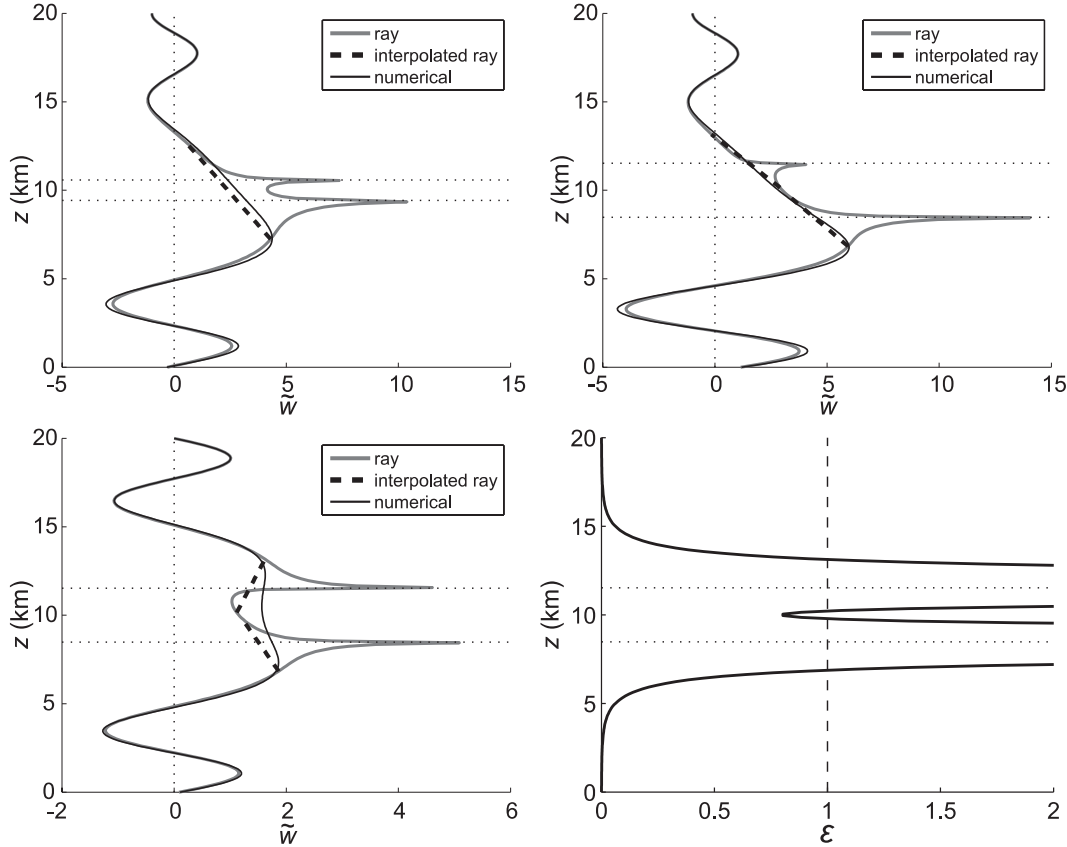
FIG. 3. Examples of the interpolated ray solution for $\tilde{w}$, without wind curvature effects. Turning-point heights are indicated by horizontal dotted lines. (top) Same cases as in the respective panels of Fig. 2. (bottom left) This illustrates a relatively large error in the interpolated ray solution, showing the imaginary part of $\tilde{w}$ for a horizontal wavelength is 14 km. (bottom right) The slowly varying parameter ϵ of (28) for the solution in the bottom left panel.

to be accurate for four-turning-point cases either, contrary to what we find in the upper two rows of Fig. 4. More work is needed to determine the factors that affect the accuracy of two-turning-point theory in these cases.

In the rest of this paper, we always use the two-turning-point interpolated ray solution, despite its poor accuracy in some cases.

5. Other effects needed for mountain-wave simulations

a. Wave reflection from the ground

Mountain waves that reflect from a turning point return to the ground, where they reflect upward again. We have not yet taken into account the contribution from these ground-reflected waves. A way to do so is given in Broutman et al. (2006) and is summarized next.

Each reflection from the ground generates a new incident wave, with a phase shift and a change in amplitude relative to the original incident wave. The phase shift is due to the total phase change in propagating from the ground to the lower turning point and then back to the ground again, including the phase shift of $-\pi/2$ at the turning point and the phase shift of π for reflection at the ground. The total phase shift is then

$$\Phi = 2 \int_0^{z_1} m \, dz + \pi/2 - 2\sigma, \qquad (30)$$

where σ is defined in (11). As noted below (11), σ is small and only has a slight effect (at most a few percent) on the results below.

For two turning points, the change in amplitude is given by

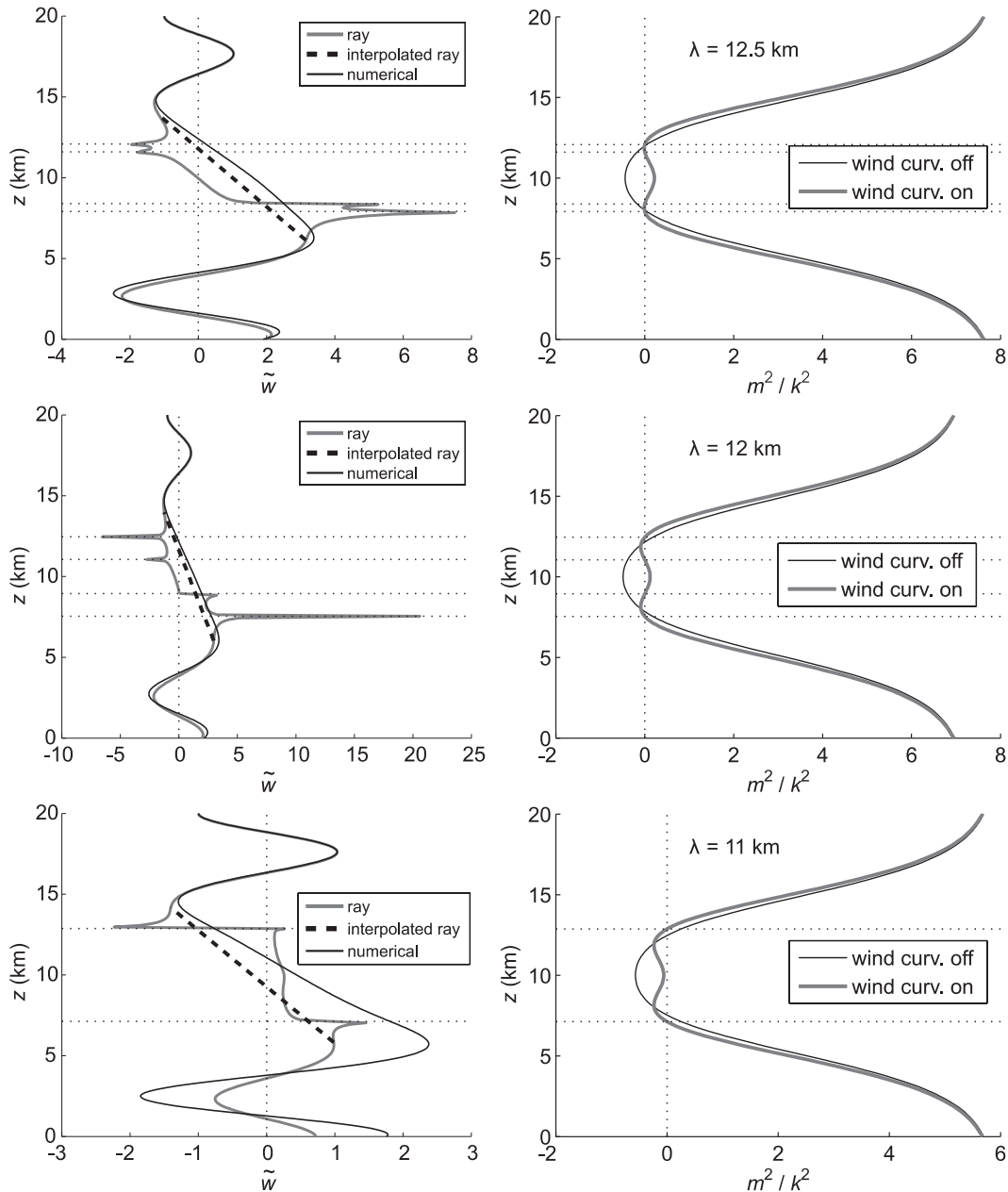$$R \equiv |w_r|/|w_i| = e^Q / (e^{2Q} + 1)^{1/2}. \qquad (31)$$

FIG. 4. Examples of the interpolated ray solution for $\tilde{w}$, with wind curvature effects: (left) solutions for the real part of $\tilde{w}$; (right) profiles of m^2 (normalized by k^2) corresponding to the left panels. Horizontal dotted lines indicate turning-point heights. Included for comparison is the m^2 profile without wind curvature (thin line). The horizontal wavelength λ in each calculation is indicated in the m^2 plot.

This reflection coefficient is the ratio of the ray amplitudes for the reflected and incident wave solutions of (9)–(10). As the distance between the two turning points widens, Q increases and R approaches unity.

To incorporate n_r reflections from the ground, we take the solutions for $\tilde{w}$ obtained above (ray, uniform, numerical) and multiply each by

$$S = \sum_{n=0}^{n_r} R^n e^{in\Phi}. \qquad (32)$$

The number of ground reflections n_r depends on the time at which we evaluate the solution and can be computed from the group velocity for each ray. The
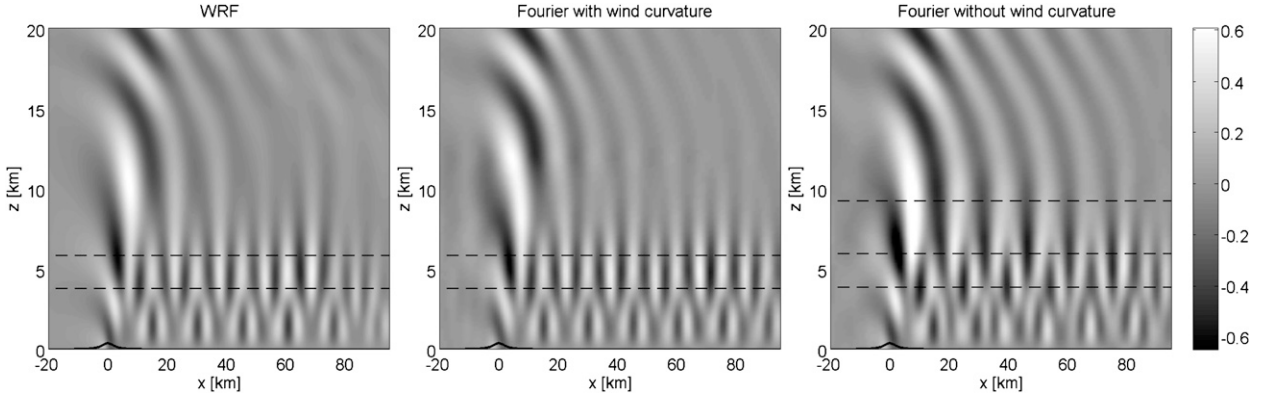
FIG. 5. The solution $w(x, z)$ in m s^{-1} at $t = 4$ h for the sech-squared wind profile: (left) WRF; (middle) interpolated ray with wind curvature; (right) interpolated ray without wind curvature. Horizontal dotted lines indicate the turning-point locations for the resonant modes given in (38)–(41). The mountain profile (36) is also shown, amplified by a factor of 4 for visibility.

time that it takes a wave group to propagate from the ground to the lower turning point and back to the ground is

$$T = 2 \int_0^{z_1} c_g^{-1} dz, \tag{33}$$

where c_g is the vertical group velocity. At time t, the number of ground reflections can be approximated as t/T rounded to the nearest integer. This approach was tested for an idealized case by Broutman et al. (2006) and was used in the Jan Mayen simulation of EB06.

b. Waves with one or no turning points

The solution for a Fourier component with only one turning point involves the Airy function. It is given in the appendix of EB06 and will not be repeated here. The solution for a Fourier component without turning points is

$$\tilde{w} = - i\hat{\omega}\tilde{h}(m_0/m)^{1/2} e^{iq}, \tag{34}$$

where $q = \int_0^z m \, dz$ and m_0 is m at $z = 0$. This satisfies the lower boundary condition (3).

c. Anelastic scaling

So far we have made the Boussinesq approximation. From here on, we include anelastic effects with the usual density scaling of the previously derived expressions:

$$\tilde{w} \rightarrow (\rho_0/\rho)^{1/2} \tilde{w}, \tag{35}$$

where $\rho(z) = \rho_0 \exp(-z/H_d)$ is the mean density and ρ_0 refers to its value at $z = 0$. We use the density scale height $H_d = 7.5$ km. Anelastic corrections to the dispersion relation (2), involving H_d, were found to be unimportant in the following examples. The results in

this paper are based on the Boussinesq dispersion relation (2).

6. Mountain waves in a sech-squared wind

We first consider a two-dimensional example, with wind shear given by the profile (26) and a constant $N = 0.015$ s^{-1}. The topography is

$$h = h_0/(1 + x^2/L^2), \tag{36}$$

with $h_0 = 100$ m and $L = 2.5$ km.

The Fourier solution is computed from (8)–(10) and (29) for the trapped waves and from (34) for the propagating waves. The grid has 512 points in x, with a grid spacing of 1 km, and 101 points in z with a spacing of 200 m. The solution is calculated at $t = 4$ h. The time affects the number of ground reflections for the trapped waves; see n_r in (32).

We also show a numerical solution using the Weather Research and Forecasting (WRF) model, a mesoscale model described in Skamarock et al. (2005). The grid for this computation has 480 grid points in x with a grid spacing of 250 m, and 301 grid points in z with a spacing 100 m. A sponge layer starts at a height of 20 km.

Figure 5 shows the (left) WRF solution and (middle), (right) Fourier solution with and without wind curvature effects, respectively. Wind curvature is included or omitted by setting $\alpha = 1$ or $\alpha = 0$, respectively, in (2). The horizontal lines are turning-point heights for the resonant modes and are discussed below.

When wind curvature is included, there are, out of a total of 256 horizontal wavenumbers, 40 for which the waves are vertically propagating without turning points. There are 80 horizontal wavenumbers for which the waves have turning points, and of these, 5 have four turning points and 75 have two turning points. (The

other horizontal wavenumbers correspond to evanescent waves and are ignored.) The waves with four turning points have horizontal wavelengths in the range of about 11.4–12.5 km. The waves with two turning points have shorter horizontal wavelengths. When wind curvature is omitted, these numbers change to 30 propagating and 90 trapped horizontal wavenumbers. All trapped waves then have two turning points and horizontal wavelengths less than 16.5 km.

Of the two Fourier solutions, the one with wind curvature (Fig. 5, middle) is in better agreement with WRF. The correlation coefficient for the WRF and Fourier solutions increases from about 0.57 without wind curvature to about 0.86 with wind curvature.

The differences between the Fourier solutions with and without wind curvature can be explained by considering the resonant modes. These are defined here as those waves that have a phase change Φ in (30) that is a multiple of 2π. For such Fourier components there is perfect constructive interference between the associated rays [i.e. those leaving the ground for the first time and those repeating their paths (in Fourier space) after each ground reflection].

For the Fourier solution with wind curvature, there are two resonant modes resolved by the present grid. Their horizontal wavelengths λ_{res} and the corresponding (lower) turning-point heights z_{res} were computed numerically to be (in kilometers)

$$\lambda_{res} \simeq 5.1, 7.5, \tag{37}$$

$$z_{res} \simeq 3.8, 5.8, \quad \text{and} \tag{38}$$

$$n_r = 7, \quad 7. \tag{39}$$

Here, n_r refers to the number of ground reflections at $t = 4$ h, as used in (32).

For the Fourier solution without wind curvature, there are three resonant modes:

$$\lambda_{res} \simeq 5.0, \ 7.1, \ 15.9, \tag{40}$$

$$z_{res} \simeq 3.9, \ 6.0, \ 9.2, \quad \text{and} \tag{41}$$

$$n_r = 7, \quad 6, \quad 3. \tag{42}$$

The heights z_{res} are indicated by the horizontal dashed lines in Fig. 5. For the WRF solution, the heights in (38) are plotted.

The presence of a third resonant mode with $\lambda_{res} \simeq 15.9$ km in the case without wind curvature seems to explain the differences in the two Fourier solutions of Fig. 5. At heights below 6 km, the Fourier solution without wind curvature shows longer horizontal scales than the

Fourier solution with wind curvature, consistent with its longer resonant mode and with the interference of three, rather than two, resonant modes. At heights above 6 km, the Fourier solution without wind curvature has larger wave amplitudes because the third resonant mode has a turning-point height near 9-km altitude. Because this turning point is close to the peak of the wind jet, there is significant transmission of this resonant mode through the wind jet.

The ratio of transmitted to incident wave amplitude is $T = [1 + \exp(2Q)]^{-1/2}$. This is derived from the ray solution (8), (9), with Q given by (7). Thus, small values of Q mean significant transmission. The values of Q corresponding to the three resonant modes in (40) are, respectively,

$$Q \equiv \int_{z_1}^{z_2} |m| \, dz \simeq 11, \ 5.2, \ 0.14. \tag{43}$$

Of these, only the 15.9-km mode has a significant value of $T \simeq 0.65$. At $z = 20$ km in the solution without wind curvature (right panel of Fig. 5) the first four downwind crests are separated by about 15 km, close to the resonant value.

For the solution with wind curvature (middle panel of Fig. 5), the downwind crests at $z = 20$ km are separated by the slightly smaller distance of about 12–14 km. This may be related to the fact that adding wind curvature shortens the maximum horizontal wavelength for the trapped solutions. Without wind curvature, this maximum wavelength is about 16.5 km. With wind curvature, the maximum wavelength falls to 12.5 km.

Above the wind jet, and downwind from the mountain, there is also a contribution to the wavefield from waves that just miss having turning points. These waves are advected downwind as they refract to a small wavenumber near the tip of the wind jet. They have less than half the amplitude of the contribution from waves that tunnel through the wind jet. We can see this by separately plotting the wavefield due to the propagating waves and due to the trapped waves. This is shown in Fig. 6.

7. Mountain waves over Jan Mayen

We next consider a three-dimensional case of mountain waves generated by the island of Jan Mayen in the far North Atlantic. The problem was studied by EB06 using a Fourier solution without two-turning-point effects. As in EB06, we use radiosonde winds and stratification for 25 January 2000 and realistic topography. There is a wind jet centered at about 10-km altitude.
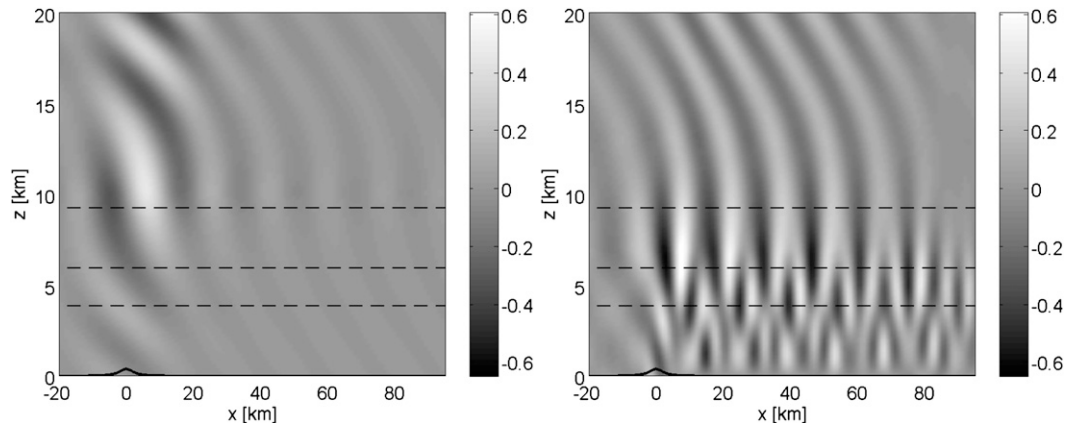
FIG. 6. The vertical velocity $w(x, z)$ in m s^{-1} for (left) vertically propagating waves and (right) vertically trapped waves, for the Fourier solution without wind curvature. Horizontal dashed lines indicate turning-point heights for the resonant modes.

The zonal wind component is plotted in the right panel of Fig. 1. For more details, see EB06.

We computed the Fourier solution on a grid with 1024 points in x, 512 points in y, and a grid spacing of 1 km in each direction. For this grid and the radiosonde wind and stratification profiles, there are about 37 000 Fourier components that correspond to stationary mountain waves. Of these, about 23 000 have at least one turning point, and of these about 21 000 have two or more turning points. These numbers vary, depending on how much smoothing is applied to the background wind and stratification profiles and on how the background wind and stratification is approximated at heights below the mountain top.

We limit the number of two-turning-point solutions we need to calculate by considering the integral Q in (7). As evident from the discussion below (43), large values of Q correspond to waves that are mostly reflected from the wind jet, with little transmission through the wind jet. Thus we compute two-turning-point solutions only for waves with $Q < 3$. Horizontal wavenumbers with higher values of Q are treated here as one-turning-point problems, using an Airy function solution up to a height midway between the two turning points. Above that height, these wavenumbers are ignored because the exponential decay between the turning points is large by that point. This is the procedure used in EB06 for all horizontal wavenumbers with two or more turning points.

There are about 6000 horizontal wavenumbers with $Q < 3$. These are treated with the interpolated ray solution (29). The three-dimensional solution is calculated from the ground to a height of 20 km at 1-km intervals. Only one vertical cross section is shown here.

The total computation time on a 2-GHz processor is about 3 min, including just under 1 min for the two-turning-point calculation.

The Jan Mayen solutions of EB06 are shown in the top row of Fig. 7. These were computed by (upper left) the mesoscale model WRF and (upper right) the Fourier method without two-turning-point effects. The island of Jan Mayen is centered at the origin of the horizontal axis.

The Fourier solution based on the interpolated ray solution is shown in the lower left panel of Fig. 7. Here we see that there is much better agreement with the WRF results when nearby turning-point effects are included in the Fourier method, both in the amplitude of the transmitted waves above the wind jet and in the associated reduction of the wave amplitude with distance below the wind jet. Wind curvature, included in the calculation for the lower left panel, also has a noticeable effect. The Fourier solution without wind curvature is shown in the lower right panel of Fig. 7. Note that the dominant horizontal wavelength of the trapped waves below about 10-km height is somewhat shorter than in the WRF result or in the Fourier solution with wind curvature (lower left panel).

The difference between the calculations with and without wind curvature in Fig. 7 is mainly a small change in the dominant wavelength of the downwind wavefield. Downwind of the mountain (at, say, $z = 5$ km), there are about four and one-half wave crests in the calculation with wind curvature (lower left panel) and five crests in the calculation without wind curvature (lower right panel). In three dimensions, there is a continuum of resonant wavenumbers in k, l space, as shown in Fig. 10 of EB06. Thus, small changes in the dispersion relation
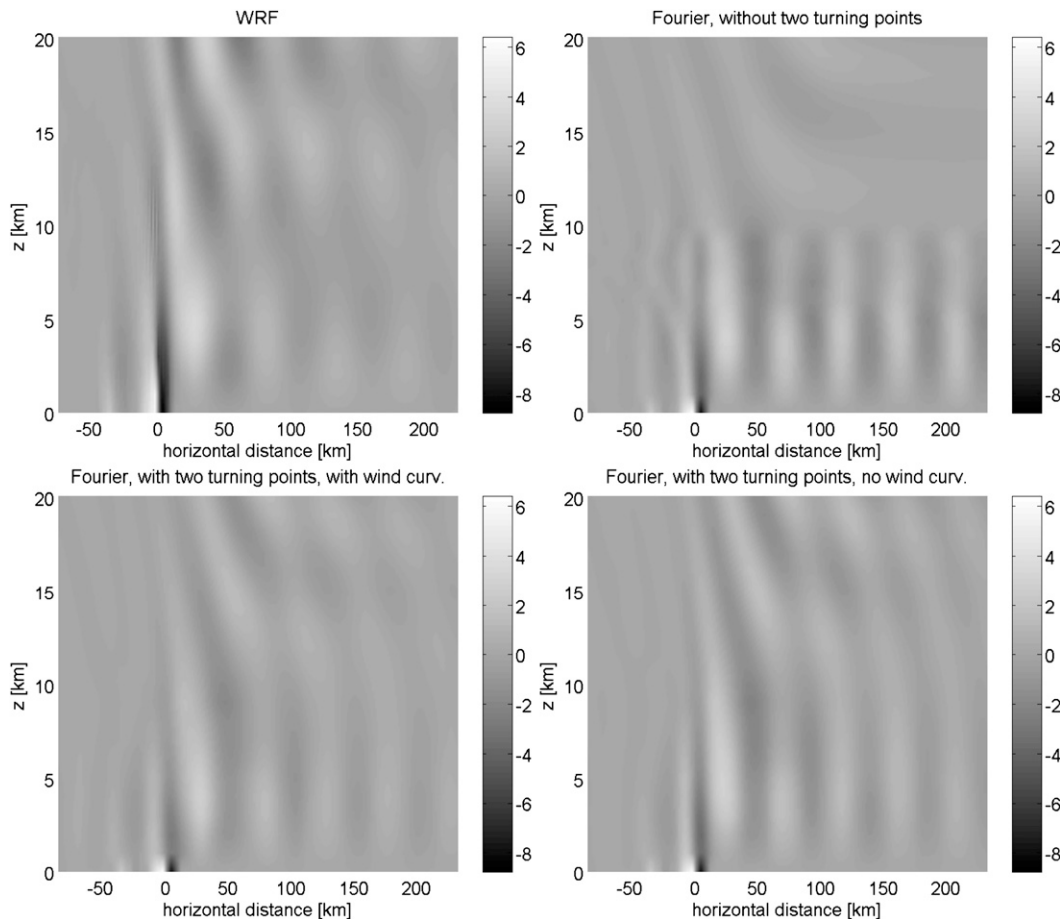
Fig. 7. Vertical cross sections of the vertical velocity $w(x, z)$ in m s^{-1} at $t = 4$ h for mountain waves generated by the island of Jan Mayen. (top) The WRF solution and Fourier solution of EB06. (bottom) The Fourier solutions that include two turning-point effects, both (lower left) with and (lower right) without wind curvature. The horizontal distance on the axis refers to a direction that is 36° north of eastward (see Fig. 8 of EB06).

due to wind curvature lead, in general, to small changes in the resonant horizontal wavenumber.

In two dimensions, as in our earlier example of Fig. 5, the resonant wavenumbers are discrete. If one of those resonant wavenumbers has a turning point near the crest of the wind jet, a small change in the dispersion relation can eliminate that resonance. The corresponding rays then change from vertically trapped to vertically propagating and no longer contribute as strongly to the downwind wavefield below the wind jet.

Thus, in our examples, we find a difference between the effects of wind curvature in two and three dimensions. In two dimensions, where the resonant wavenumbers are discrete, the effects of wind curvature can change the number of resonant horizontal wavenumbers. In three dimensions, where the resonant wavenumbers are continuous, the inclusion of wind

curvature slightly changes the wavenumber at resonance.

8. Discussion

We dealt with the breakdown of ray theory near closely spaced turning points in a wind jet by linearly interpolating the ray solution across the turning-point region. This involved ray solutions from the two-turning-point theory of Fröman and Fröman (1970), which were used here even when there were four turning points in the wind jet region.

For cases with two turning points, this procedure worked well, as illustrated in Fig. 3 for a sech-squared wind profile. The success of the interpolation is due in part to having a reliable criterion, (27) or (28), to identify where the ray solution breaks down and should be replaced by the interpolated values.

For cases with four turning points, which arise when wind curvature terms are included in the dispersion relation (2), this procedure produced accurate results for some Fourier components. This is illustrated in the top two rows of Fig. 4. But for other Fourier components, the error was significant, as illustrated in the bottom row of Fig. 4. More study is needed to understand which cases work, and why they should work at all. The ray solution for four turning points derived by Fröman and Dammert (1970) may be helpful in this regard, but it was not implemented here.

Another area for further study is waves that just miss having turning points in the wind jet. We approximated these Fourier components as purely upward-propagating waves [see (34)] when actually they would generate significant partial reflection from the wind jet. Thus, the wave amplitudes for these Fourier components were probably overestimated above the wind jet and underestimated below the wind jet. Partial reflection occurs to some extent for all wave propagation in a variable medium. For waves that just miss turning points, the turning points are positioned near the real axis in the complex z plane, and the strength of the partial reflection is a function of the distance from these complex turning points to the real axis. The theory is given in Fröman and Fröman (1970).

Despite the shortcomings in our approach, it did lead to an improved comparison with the results of a mesoscale model. The effects of nearby turning points were important in both examples, as were the effects of wind curvature in the wind jet.

Other methods for treating nearby turning points may turn out to be more efficient. Our aim here was to show what is required to implement ray solutions for nearby turning points. We have not experimented at all with solutions to (1) based on a layered approximation for the background (e.g., Smith et al. 2002; Sutherland and Yewchuk 2004; Brown and Sutherland 2007), and we have not experimented much with the numerical integration of (1). In Nault and Sutherland (2007), a numerical integration of an equation similar to (1) took about 1 s of computation time per Fourier component on a standard processor, and accordingly the integration of a 300×300 grid of Fourier components took about 1 day to complete. However, if a portion of the Fourier spectrum is selected such that the same integration step size is appropriate for all of the selected Fourier components, the integration could be vectorized with a great reduction in overall computing time. NaSu have begun to experiment with a vectorizable Heun's method for a problem with nearby points. Our limited tests with this method also suggest that it might be effective. More testing is required, and the present solutions should be useful for comparison and interpretation.

REFERENCES

Abramowitz, M., and L. A. Stegun, 1964: *Handbook of Mathematical Functions.* National Bureau of Standards, 1046 pp.

Bacmeister, J., 1993: Mountain-wave drag in the stratosphere and mesosphere inferred from observed winds and a simple mountain-wave parameterization scheme. *J. Atmos. Sci.,* **50,** 377–399.

Baines, P. G., 1995: *Topographic Effects in Stratified Fluids.* Cambridge University Press, 482 pp.

Berry, M. V., 1969: Uniform approximation: A new concept in wave theory. *Sci. Prog.,* **57,** 43–64.

——, and K. E. Mount, 1972: Semiclassical approximation in wave mechanics. *Rep. Prog. Phys.,* **35,** 315–397.

Broutman, D., J. W. Rottman, and S. D. Eckermann, 2003: A simplified Fourier method for nonhydrostatic mountain waves. *J. Atmos. Sci.,* **60,** 2686–2696.

——, J. Ma, S. D. Eckermann, and J. Lindeman, 2006: Fourier-ray modeling of transient trapped lee waves. *Mon. Wea. Rev.,* **134,** 2849–2856.

Brown, G. L., and B. R. Sutherland, 2007: Internal wave tunnelling through non-uniformly stratified shear flow. *Atmos.–Ocean,* **45,** 47–56.

Eckermann, S. D., D. Broutman, J. Ma, and J. Lindeman, 2006: Fourier-ray modeling of short-wavelength trapped lee waves observed in infrared satellite imagery near Jan Mayen. *Mon. Wea. Rev.,* **134,** 2830–2848.

——, J. Ma, D. L. Wu, and D. Broutman, 2007: A three-dimensional mountain wave imaged in satellite radiance throughout the stratosphere: Evidence of the effects of directional wind shear. *Quart. J. Roy. Meteor. Soc.,* **133,** 1959–1975.

Einaudi, F., and C. O. Hines, 1970: WKB approximation in application to acoustic-gravity waves. *Can. J. Phys.,* **48,** 1458–1471.

Fritts, D. C., and M. J. Alexander, 2003: Gravity wave dynamics and effects in the middle atmosphere. *Rev. Geophys.,* **41,** 1003, doi:10.1029/2001RG000106.

Fröman, N., and P. O. Fröman, 1965: *JWKB Approximation: Contributions to the Theory.* North-Holland, 138 pp.

——, and Ö. Dammert, 1970: Tunneling and super-barrier transmission through a system of two real potential barriers. *Nucl. Phys.,* **147A,** 627–649.

——, and P. O. Fröman, 1970: Transmission through a real potential barrier by means of certain phase-integral approximations. *Nucl. Phys.,* **147A,** 606–626.

——, and ——, 2002: *Physical Problems Solved by the Phase-Integral Method*. Cambridge University Press, 214 pp.

Heading, J., 1962: *An Introduction to Phase-Integral Methods*. John Wiley, 160 pp.

Kravtsov, Y. A., and Y. I. Orlov, 1999: *Caustics, Catastrophes, and Wave Fields*. Springer, 216 pp.

Nault, J. T., and B. R. Sutherland, 2007: Internal wave transmission in nonuniform flows. *Phys. Fluids,* **19,** 016601, doi:10.1063/1.2424791.

——, and ——, 2008: Beyond ray tracing for internal waves. I. Small amplitude anelastic; waves. *Phys. Fluids,* **20,** 106601, doi:10.1063/1.2993167.

Razavy, M., 2003: *Quantum Theory of Tunneling*. World Scientific, 549 pp.

Skamarock, W. C., J. C. Klemp, J. Dudhia, D. O. Gill, D. M. Barker, W. Wang, and J. G. Powers, 2005: A description of the Advanced Research WRF version 2. NCAR Tech. Note NCAR/TN-468+STR, 88 pp.

Smith, R. B., S. Skubis, J. D. Doyle, A. S. Broad, C. Kiemle, and H. Volkert, 2002: Mountain waves over Mont Blanc: Influence of a stagnant boundary layer. *J. Atmos. Sci.,* **59,** 2073–2092.

Sutherland, B. R., and K. Yewchuk, 2004: Internal wave tunnelling. *J. Fluid Mech.,* **511,** 125–134.

Teixeira, M. A. C., P. M. A. Miranda, and M. A. Valente, 2004: An analytical model of mountain wave drag for wind profiles with shear and curvature. *J. Atmos. Sci.,* **61,** 1040–1054.